







## Article

# Longitudinal DC Discharge in a Supersonic Flow: Numerical Simulation and Experiment

Alexander Firsov , Valentin Bityurin , Dmitriy Tarasov , Anastasia Dobrovolskaya , Roman Troshkin   
and Aleksey Bocharov 

Joint Institute for High Temperatures of the Russian Academy of Sciences (JIHT RAS), 125412 Moscow, Russia

\* Correspondence: af@jht.org

**Abstract:** This work focuses on detailed descriptions of DC discharge properties in supersonic airflow and its applicability in combustion simulations. Due to the complexity of obtaining most of the data in the experiment, our experimental research was supplemented by a numerical simulation. Two packages, i.e., FlowVision (fast commercial CFD for 3D engineering) and Plasmaero (2D scientific code developed in JIHT RAS for MHD tasks), were used for modeling the arc DC discharge in a supersonic flow at Mach ( $M$ ) = 2. Both will be considered for further use in plasma-assisted combustion modeling, so it is important to validate both codes using experimental data from the model configuration with discharge. Axisymmetric geometries of experiments with two coaxial electrodes located parallel to the flow were chosen to avoid the appearance of the current channel part perpendicular to the flow and the corresponding discharge pulsations. Such geometries allow performing numerical simulations in 2D formulation, making it possible to compare the results obtained in the experiments and calculations. As a result of this work, two-dimensional distributions involving temperature, current density, chemical composition, and other discharge and flow parameters were obtained for arc DC discharges 0.5–7 A in a supersonic flow ( $P_{st} = 22$  kPa,  $T = 170$  K,  $V \sim 500$  m/s). Good qualitative agreement between experimental and numerical results was achieved. The production of a significant amount of atomic oxygen, which accelerates combustion, was noted.

**Keywords:** DC discharge; arc discharge; supersonic flow; experiment; numerical simulation



**Citation:** Firsov, A.; Bityurin, V.; Tarasov, D.; Dobrovolskaya, A.; Troshkin, R.; Bocharov, A. Longitudinal DC Discharge in a Supersonic Flow: Numerical Simulation and Experiment. *Energies* **2022**, *15*, 7015. <https://doi.org/10.3390/en15197015>

Academic Editor: Adonios Karpetis

Received: 25 August 2022

Accepted: 19 September 2022

Published: 24 September 2022

**Publisher's Note:** MDPI stays neutral with regard to jurisdictional claims in published maps and institutional affiliations.



**Copyright:** © 2022 by the authors. Licensee MDPI, Basel, Switzerland. This article is an open access article distributed under the terms and conditions of the Creative Commons Attribution (CC BY) license (<https://creativecommons.org/licenses/by/4.0/>).

## 1. Introduction

Globally, researchers are studying the interaction between electrical discharge and a high-speed flow, in relation to two major problems: (1) plasma aerodynamics/plasma flow control [1–3] and (2) mixing problems [4–6], ignition, and flame stabilization [7,8] in a supersonic flow using discharge, known as plasma-assisted combustion [9], which is one fundamental in the development of a ramjet or a scramjet engine [10,11].

The first group of tasks consists of numerous research studies on subsonic flow devoted to boundary layer transitions and separation control. Fundamental research on plasma actuators, including the most popular DBD, continues; moreover, new (and previously unaccounted for) properties are being discovered [12]. In the applied works, features on the influence of flow are presented, for example, in the work by [13], a mechanism of hydrodynamic noise generation in a boundary layer by a dielectric barrier discharge was considered, which can be key in further attempts to influence the boundary layer with this type of actuator.

The second significant part of the research on plasma aerodynamics is related to the control of the shock-wave structure in a supersonic flow. It is well-known that the pulsed energy input in the discharge is accompanied by the birth of a shock wave and can affect the structure of the external flow [14,15] or the flow in the channel [16]; in this case, the duration of the energy input can be less than a microsecond, and the restoration of the flow structure requires more than 100  $\mu$ s. When controlling the flow near the compression

surface (in the air intake), the energy input from the plasma actuator can be pulsed [17], or constantly operated, while in both cases, the flow structures change significantly, allowing for optimizing the operation of the air intake in an off-design mode [18]. The change in the flow structure when switching the plasma actuator takes several hundred  $\mu\text{s}$  for a characteristic size of the observation zone of about 100 mm [19].

One of the key options for a plasma actuator in a supersonic flow is a direct current discharge (or an arc discharge), which is used to control the flow [18,19] and in problems related to plasma-assisted combustion [8,20,21]. In the case of combustion, the energy input to the discharge, in recent works [21], is several percentage points of the power released during combustion. Therefore, this approach looks promising. Studies on the properties of such a discharge in a supersonic flow began in the 1950s and 1960s [22], with the development of diagnostic tools and computational–theoretical approaches; research continues on the properties of the discharge [23], various effects of gas jets [24], and magnetic field [25] influences on the discharge. In the vast majority of studies, a discharge of a complex shape is considered, which makes it difficult to analyze and interpret the results. Therefore, the axisymmetric statement of the discharge problem, without a part of the current channel perpendicular to the flow considered in this paper, is relevant.

To obtain complete spatial distributions of such properties, such as velocity, pressure, and temperature in a supersonic airflow, it is useful to perform a numerical simulation. There are many approaches to consider discharge plasma in a numerical simulation. The simplest way to simulate the impact of the discharge on the flow, which does not include MHD (magnetohydrodynamic) equations, is to use a volumetric heat source [19,26]. However, this method has serious limitations. It is difficult to set the real spatial distribution of the energy input and to take into account the change of the discharge shape or length that takes place in the experiment and, as a result, makes it interact with the flow of the fuel–air mixture. The discharge approximately follows the flow lines, which is clearly seen in the Supplementary Material of the article [27]. Complex modeling of the electric discharge was carried out earlier using various electrodynamic models. To simplify the model, two-dimensional modeling is often used. In [28,29], the discharge cross-section was simulated for a case involving a discharge motion under a constant magnetic field. To obtain the spatial distributions of the discharge characteristics in a supersonic flow, the problem was formulated in [30] in the axisymmetric approach for low currents. In [31], a numerical simulation of a configuration, in which a fast-moving arc discharge appeared between two extended electrodes, called a rail plasma actuator, was performed. The object of the simulation was the repeated breakdown of the discharge; however, all calculations were performed in the plane of the discharge. A re-breakdown (or restrike) effect appears if a current channel has a part that is perpendicular to the flow; in such a situation, it is important to provide a restrike model [32]. However, this significantly complicates the simulation and affects the stability of the parameters in the experiment.

In this work, the re-breakdown (or restrike) effect was not considered for simplification of the discharge geometry or further comparison of the experimental results. Using different approaches, a straight 30 mm long discharge was used to obtain a detailed description of the DC discharge properties in supersonic airflow. Axisymmetric geometries of experiments with two coaxial electrodes located parallel to the flow were chosen to avoid the appearance of the current channel part perpendicular to the flow and corresponding discharge pulsations. Such geometries allow performing numerical simulations in 2D formulation, making it possible to compare the results obtained in the experiments and calculations. Two packages, i.e., FlowVision and Plasmaero, were used for modeling the arc DC discharge in a supersonic flow at Mach ( $M$ ) = 2. FlowVision was applied here to make a 3D simulation with an unsteady DC discharge. Plasmaero was applied due to the detailed plasma chemistry available in the discharge simulation.

## 2. Experimental Setup and Measurement Methods

To obtain detailed information about the local characteristics of the discharge and gas flow near the discharge, we considered a direct current discharge in the simplest formulation: the core of a supersonic flow (i.e., far from the walls), in a configuration between two coaxial electrodes located parallel to the flow (to ensure the absence of the current channel perpendicular to the flow). Such a configuration was realized in an experiment in a supersonic wind tunnel IADT-50 of the JIHT RAS. A discharge with a current of 0.5–7 A was ignited in the core of the supersonic flow ( $M = 2$ ,  $V \sim 500$  m/s,  $T_g = 170$  K,  $P_{st} = 22$  kPa) between thin coaxial electrodes with a distance (from the ends of the electrodes) of 30 mm. The control of the current was conducted by replacing the ballast resistance  $R_1$ . The geometry of the experiment was chosen considering the 2D simulation approach. In the chosen configuration, two electrodes were installed coaxially—the first one (upstream) was steel with a diameter of 1 mm, the second (downstream) was copper (2 mm); the third (initiating) electrode was curved, and was intended for the initial breakdown, i.e., the start of the discharge, which ignited in the form of a loop carried by the flow; when it reached the downstream electrode, it switched to the longitudinal mode. The geometry of the third electrode ensured the minimum intensity of the shock wave incident from the electrode into the discharge operation region. Thus, the presence of the third electrode could be neglected in the simulation. Such a configuration was recognized as generally successful and satisfied the wishes of the theoretical group. However, at high currents (4–6 A), a tip of the front steel electrode heated up strongly and was destroyed, which hampered the spectroscopic measurements. Therefore, the next configuration was made using the upstream tungsten electrode, on which experiments were performed at high currents. In this case, no destruction of the electrode was observed, which was recorded by a high-speed camera. The electrical circuit and the basic configuration of the electrodes are shown in Figure 1.

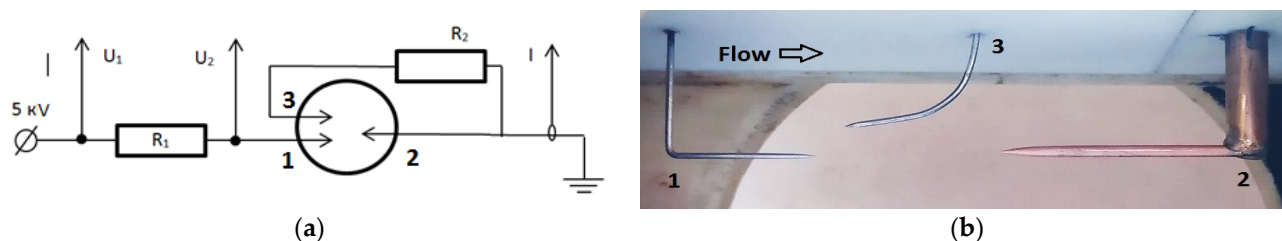


**Figure 1.** (a) Scheme of discharge supply and electrical measurements. (b) The geometrical configuration of electrodes. 1—upstream, 2—downstream, and 3—initiating electrode.

The discharge was powered from a constant voltage source of 5 kV through a ballast resistance that regulated the discharge current. In the experiment, electrical measurements were performed, the discharge current varied in the range of 0.5 to 6 A, and the obtained discharge voltage was, respectively, from 900 to 280 V. During the experiments, high-speed shooting of the discharge was carried out on a Photron S9 camera with an exposure of 1–2  $\mu$ s, the features of the flow were recorded using a high-resolution shadow system with an exposure of 100 ns (based on laser beam pulse). The spectra of the optical emission of the discharge were obtained in the range of 287–367 nm using a spectrograph based on an Oriel MS 257 monochromator (1800 lines/mm grating) and an Andor DU420 CCD camera. The temperature was determined from the optical emission of a thin cross-section of the discharge. With the help of a rotary mirror, it was possible to determine the temperatures at different points along the discharge. The scheme (of optical measurements and visualization) is shown in Figure 2.

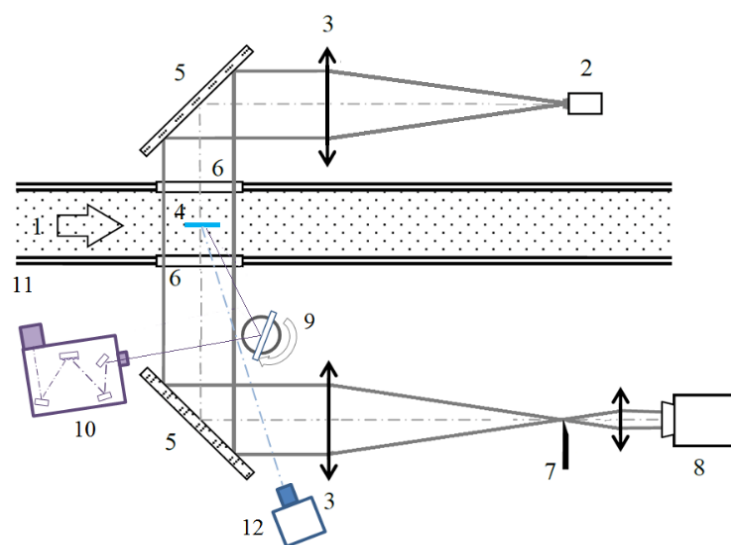


**Figure 2.** Scheme of optical measurements and visualization. 1—supersonic flow; 2—laser beam; 3—lens,  $F = 1.5$  m; 4—electric discharge DC; 5—mirror; 6—transparent window; 7—knife-edge; 8—high-speed camera; 9—rotating mirror for spectrograph; 10—monochromator; 11—spectrum camera; 12—high-speed camera.

### 3. CFD Simulation in FlowVision

#### 3.1. Equations

FlowVision is a commercial CFD code [33] in which the one-fluid model (MHD approximation) of electrodynamic was recently added by developers. This CFD code uses the 3D URANS approach and includes standard turbulence models. The turbulence model was disabled to be closer to the capabilities of Plasmaero software. Computations in FlowVision used the finite volume method and were performed using a solver of linear systems based on the algebraic multigrid (AMG) method. Calculations could be performed in parallel mode on multi-core systems and supercomputers. Second-order discretization schemes were applied to solve aerodynamic problems. Additional information could be found in the FlowVision user manual [34].

The electrodynamic model we used is described by the following equations:

$$\begin{aligned}\nabla \cdot \mathbf{j} &= 0 \\ \mathbf{j} &= \sigma \mathbf{E} \\ \mathbf{E} &= \nabla \varphi,\end{aligned}\quad (1)$$

Joule heat is calculated as:

$$Q_{\text{Joule}} = \mathbf{j} \cdot \mathbf{E} = \sigma \mathbf{E}^2, \quad (2)$$

In the implementation of the EHD process, it was supposed that dielectric permeability did not depend on the density of the medium. Boundary conditions (electric potential and current density) were used for the electrodes. These boundary conditions were set with the aid of:

$$\varphi_b = \varphi_{\text{ext}}, \quad \left( \frac{\partial \varphi}{\partial n} \right)_b = \frac{j}{\sigma}, \quad (3)$$

For the numerical simulation of an electric discharge in an air flow using a single-fluid model, it is necessary to know the thermodynamic characteristics and air transfer coefficients. In addition, the discharge temperature can reach about 8000 K at atmospheric pressure, so the physical characteristics of the gas must be known in a wide range of temperatures and pressures. The temperature dependencies of thermal conductivity  $\lambda(T)$  and specific electrical conductivity  $\sigma(T)$  are especially important for modeling the discharge

channel. In the article, we used data on the physical characteristics of air from [35], where the calculated values were adjusted according to closed forms. Their ranges were: air at pressures of 0.01–100, atmosphere and temperature at 50–60,000 K, which are several times higher than the value ranges required for the calculations. Copper was used as the electrode material, the physical characteristics of which were loaded from the FlowVision Standard Library of Substances. The approach described in this subsection was previously tested to solve the 3D task with discharge in airflow [36].

### 3.2. Calculation Domain

The flow parameters and the geometry of the problem in the calculations were identical to the experimental one. For the simulation of longitudinal axisymmetric electric discharge, a cylindrical sector with a radius of 35 mm, a height of 70 mm, and an angle of  $3.6^\circ$  was used as the calculation domain, and the task was considered in the 2D approach. The electrodes were cylindrical with conical ends. Initial and inlet boundary conditions corresponded to the experiment. At the exit from the computational domain, the free outlet boundary condition was used. On the side, faces of the sector symmetry boundary conditions were used. The remaining face, which is on the top of Figure 3, had non-reflective boundary conditions.

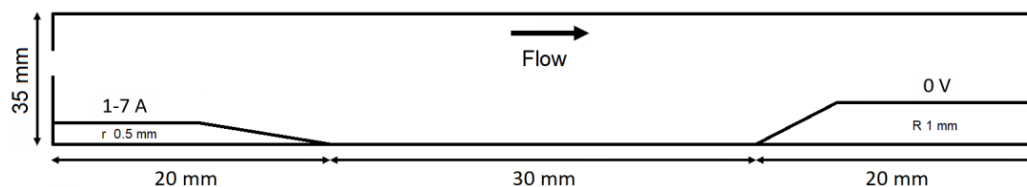


**Figure 3.** Geometry of electrode configuration for simulation in FlowVision and Plasmaero.

The input and output faces had zero gradient boundary conditions for the potential. The walls of the electrodes had boundary conditions that ensured the continuity of the electric current. The boundary conditions that were set at the far ends of the electrodes were responsible for direct currents. Therefore, for the front electrode, the boundary condition was set to a constant current  $I = 1\text{ A}, 3\text{ A}, 5\text{ A},$  and  $7\text{ A}$  with a fixed current density; for the output electrode, a constant electric potential was equal to zero. To create a current channel that connected the nearest ends of the electrodes, the temperature  $T_d = 6000\text{ K}$  was set in a thin cylinder.

The calculation used an adaptation of a rectangular Cartesian grid. The adaptation, according to the Mach number field and the manual adaptation in the selected area, was used in the project, which resulted in a spatial resolution of 80 cells per 1 mm in both directions. Thus, to achieve maximum efficiency and minimum calculation times, the total number of cells was kept at the minimum required level. The maximum number of calculation cells in the project was approximately  $1 \times 10^6$ .

## 4. CFD Simulation in Plasmaero

### 4.1. Equations

The Plasmaero software package was developed at the JIHT RAS and has been used in the last twenty years for solving hypersonic flows in electric and magnetic fields, including re-entry [37,38], plasma aerodynamics, and detailed modeling of different types of discharges [39]. During its usage—combustion, non-equilibrium, non-quasi neutral plasma models were implemented. Plasmaero applies the control volume formulation for a transport equation. The Godunov-type flux scheme [40] is applied to capture gas-dynamic discontinuities, and the Gauss theorem is used to deal with viscous fluxes. Solvers based on incomplete Cholesky factorization schemes (with preconditioning and a multigrid) [41] are applied to process low-magnetic Reynolds number electrodynamic problems. A special implicit solver is applied to solve stiff ODEs arising from chemical kinetics. Plasmaero uses structured quadrilateral grids. Typically, first- and second-order discretization schemes

are applied to solve problems of plasma aerodynamics and/or combustion. The current implementation of Plasmaero allows solving problems with discharges in a single-core mode, and aerodynamic problems in a multi-core mode. Additional detailed information could be found in reference [37].

The problem under consideration obtained the self-consistent solution of the: (I) Navier–Stokes equations for real chemically-nonequilibrium air, which was supplemented by a source term in the energy equation to take into account the Joule heat release; (II) a kinetic model of ionized air in a strong electric field (up to several hundreds of Td), with 11 components ( $N_2$ ,  $O_2$ ,  $NO$ ,  $N$ ,  $O$ ,  $N_2^+$ ,  $O_2^+$ ,  $NO^+$ ,  $N^+$ ,  $O^+$ ,  $e$ ) and 97 thermochemical reactions [42], supplemented by 5 reactions involving electrons in strong electric fields [43]; (III) equations of state for each of the components; (IV) relations for determining partial fluxes in the diffusion–drift approximation; and (V) the equation for the electric potential obtained from the condition of the conservation of the electric current. The basic equations are presented in Appendix A. There is no accounting for turbulence in Plasmaero; only 2D simulation was possible, which are drawbacks of Plasmaero. Additional information about the Plasmaero package and used models could be found in the references [30,37,39].

#### 4.2. Calculation Domain

The flow parameters in the calculations and the geometry of the problem were identical to the experimental ones and the modeling using FlowVision (Figure 3): homogeneous stationary gas flow with Mach 2, static pressure 22 kPa, and static temperature 157 K. The solution area under consideration is a meridional section of the cylindrical flow area, in which there are two coaxial conical electrodes. For the selected geometry, a parametric study was performed. The discharge was simulated for several values of the discharge current (1-3-5-7 A), and the voltage on the electrodes was automatically generated at each time step, taking into account the instantaneous distributions of the parameters of the working fluid in the entire area. The working medium was a mixture of  $0.78N_2 + 0.22O_2$  (as well as the results of its chemical transformation). The initial (and incoming) homogeneous background ionization was  $N_e = N_i = 10^{12} \text{ m}^{-3}$ .

A self-consistent solution of the above equations was performed at each moment on a  $347 \times 106$  cells structured grid with radial thickening near the symmetry axis and longitudinal thickening in the vicinity of the tops of the conical electrodes (50–15 cells per 1 mm in radial direction near axis). For each current, the calculations were carried out until a stationary solution, characterized by the voltage reaching a stationary value, required about 200  $\mu\text{s}$  for each current.

## 5. Results and Discussion

### 5.1. Featured Experiment Results

After the discharge ignition between the upstream and initiating electrodes, it was blown down by the flow (such a discharge is transverse to the flow's current path). However, after the loop contacted the downstream electrode, the discharge became a straight line, and the current and voltage of the discharge became stable and almost constant. The ignition and stable operation of the discharge are presented in Figure 4.





**Figure 4.** Photos of the discharge channel in the supersonic flow: (1,2) launch and (3) stable operation.

The discharge operation in the supersonic airflow resulted in the formation of a cone with heated gas around the discharge filament and a weak Mach cone in front of the discharge. Typical schlieren images of the supersonic flow field with and without discharge are presented in Figure 5. It is clearly seen that the cone with heated gas was slightly wider than the visible discharge channel.

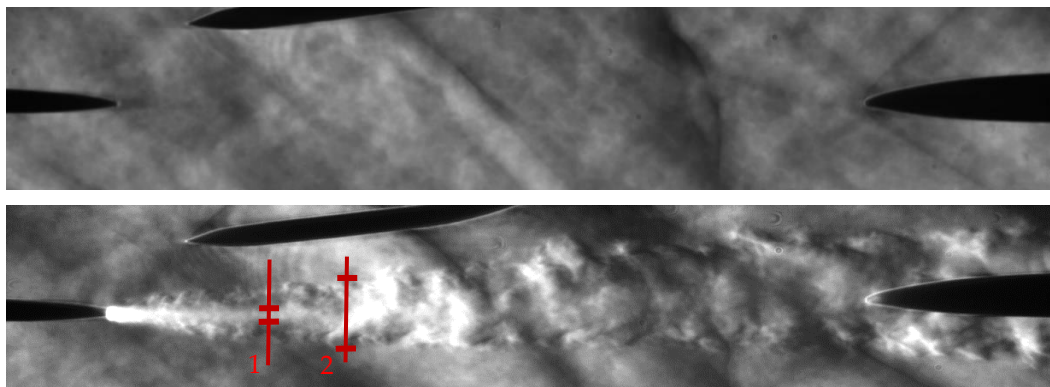


**Figure 5.** Typical schlieren images of the supersonic flow field (**top**) without discharge and (**bottom**) with discharge. 1—Discharge channel, 2—heated cone.

It is important to note that the current–voltage characteristics of the discharge obtained as a result of the experiments were in very good quantitative agreement with the results of the numerical simulations carried out (via FlowVision and Plasmaero packages), as shown in Figure 6a; the current density profiles had minor differences between FlowVision and Plasmaero. The current profiles obtained in the simulations were in good agreement with the channel diameter determined from the current channel luminosity profile on a high-speed video recording. In the experiment at 1 A, the diameter at a height of 5% of the maximum intensity was 1.2 mm, and at 6 A, it was 1.8 mm, which are closer to the diameters of the distributions presented in Figure 6b. The diameter of the thermal cone was from 3 to 5.5 mm at a distance of 25 mm from the upstream electrode at the current variation, which was also in good agreement with the simulation data. The results obtained make it possible to conclude that the experiment and simulation are in satisfactory agreement, and could allow for further comparisons and analyses of the data obtained.

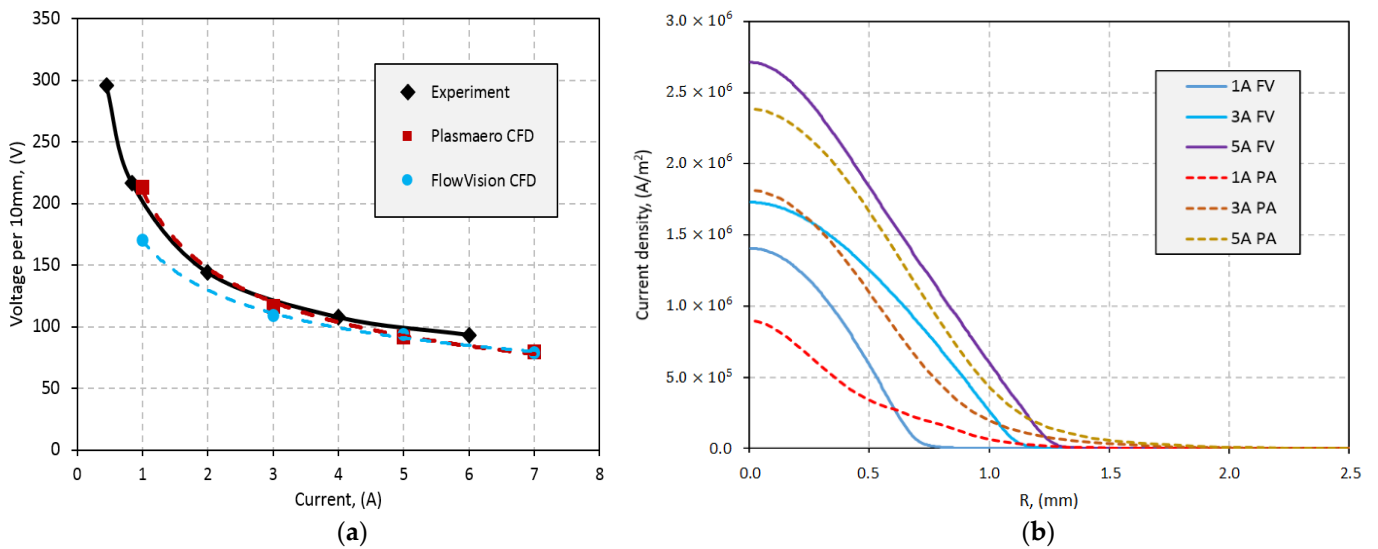


**Figure 6.** Voltage–current dependency (a) and comparison of current density profiles at  $x = 15$  mm for FlowVision and Plasmaero at 1, 3, and 5 A (b).

Temperatures in three positions of discharge filaments at different currents were obtained in the experiment using comparisons of optical emission spectra of the second positive nitrogen system  $N_2(2+)$  with modeled spectra of known rotational and vibrational temperatures (obtained using the Specair program). Thus, the temperature distributions along the discharge for each discharge current were obtained for three points—5, 15, and 25 mm. Figure 7a shows the results for the points that are 15 mm from the upstream electrodes at various currents. From the obtained data, it follows that the temperature slightly decreased along the discharge; with an increase in the discharge current, the temperature increased, and a qualitative estimate of the temperature in the discharge was obtained, which was 4000–7000 K, depending on the discharge current. When using a tungsten electrode, at a maximum current of 6 A near the tungsten electrode, metal lines were still visible on the spectrum; despite this, it was possible to process the obtained spectra.

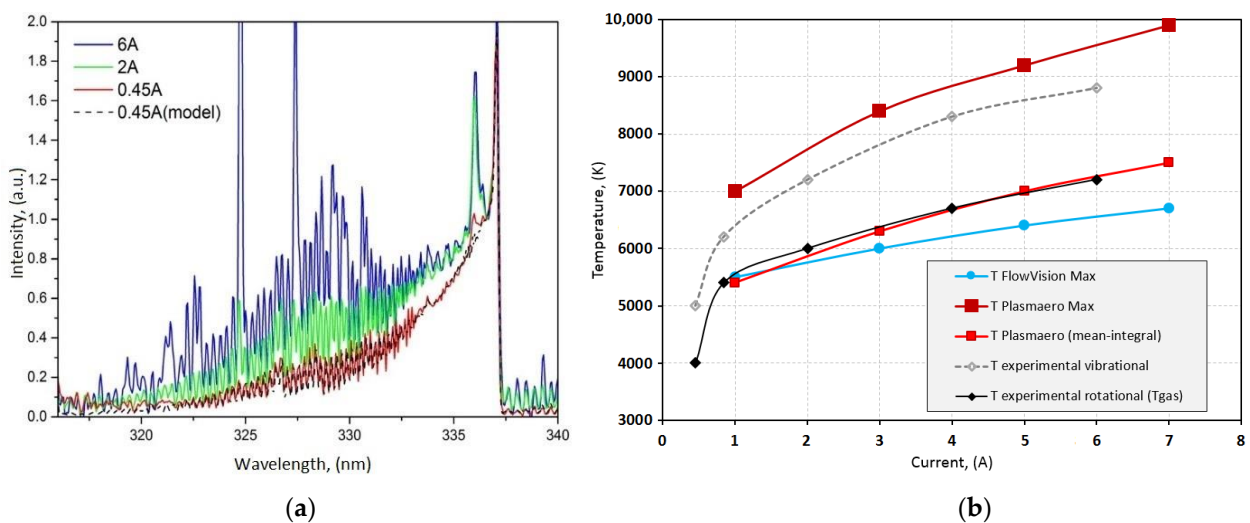


**Figure 7.** Typical spectra of discharges at the current variation (a) and comparison of the experiments and calculations by CFD temperature–current dependencies (b).

Comparisons of the obtained experimental dependencies of temperature on the current with the results from simulations performed using FlowVision and Plasmaero are shown in Figure 7b (for a point 15 mm from the electrode). The obtained temperatures have



a significant quantitative difference. It is assumed that the resulting differences between the simulation in Plasmaero and the experiment arise from the fact that the experimental spectrum was integral (averaged) along the observation line, while the maximum temperature for a given section was used as the simulation result.

Knowing the distribution of the gas temperature  $T_g$  and reduced electric field  $E/N$  along the radius in the discharge from the simulation in Plasmaero (see Figure 8), it is possible to obtain a synthetic model integrated spectrum. The typical  $E/N$  for all calculations did not exceed 100 Td (excluding the small area near the upstream electrode) and was in the range of 40–80 Td at the axis. The electron temperature distribution was calculated from the  $E/N$  distribution based on the  $T_e(E/N)$  dependency from [44] obtained by BOLSIG+ solver. The obtained  $T_e$  was in good agreement with the experimental data presented in [27,45].  $T_e(E/N)$  has an increase in the growth rate, starting with 60–70 Td, which is why  $T_e(r)$  for 1 A has a difference compared to the other distributions. The model spectrum was built for each point of the radial distribution with a step of 0.1 mm with known  $T_g$  and  $T_e$ , after which, all of the obtained spectra were added. For the resulting integrated spectrum, the closest model spectrum was selected to determine the “effective” temperature. For example, at a 5 A current, with a maximal temperature of 9200 K, the model integrated spectrum will correspond to a temperature of 7000 K, which agrees well with the experiment. The difference in temperature data between Plasmaero and FlowVision will be described in part 5.3.

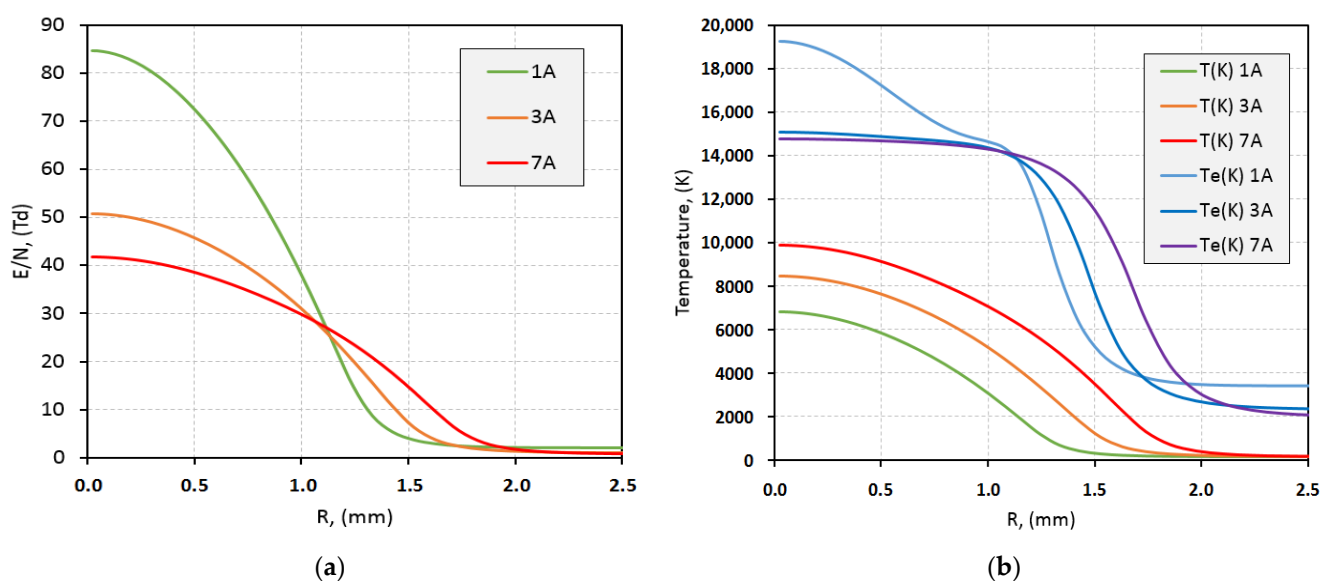


**Figure 8.** Radial profiles at a distance of 15 mm from the upstream electrode of  $E/N$  (a) and temperature/electron temperatures (b) for different currents obtained by Plasmaero.

### 5.2. Featured FlowVision Results

As a result of modeling in FlowVision, two-dimensional distributions of such physical quantities as temperature, current density, velocity, Mach number, density, and others were obtained for each discharge current. The distributions of these quantities were considered after the system reached a steady state, namely, when the voltage between the electrodes (and, hence, the energy release of the direct current discharge) and the position of the boundary of the thermal region of the discharge stabilized.

The distributions obtained in the simulations for different discharge currents were qualitatively similar; therefore, a description of the simulation results for the 3 A DC discharge will be given. In Figure 9, the temperature, velocity, Mach number, density, and current density distributions are shown in the discharge region. The discharge current created a high-temperature region surrounded by a supersonic ( $M = 2$ ) flow. The figure clearly shows that the thermal region was much larger than the current channel, which is

consistent with the experimental data. Near the electrodes (especially the upstream electrode), there was a strong increase in the current density and, as a result, in the temperature relative to the values in the middle of the discharge.

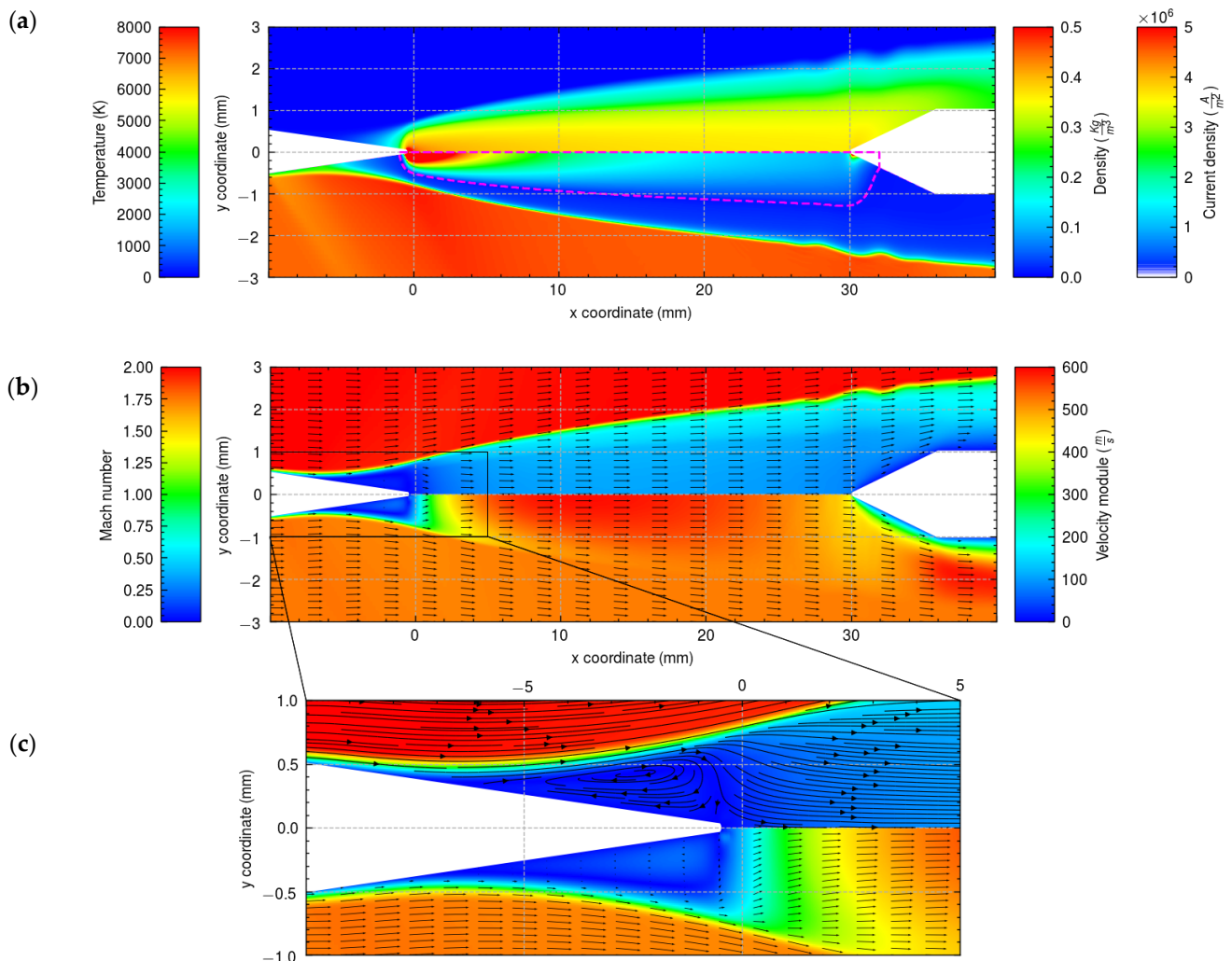


**Figure 9.** Calculation results in FlowVision for the 3 A current: (a) temperature distributions (top), as well as density (bottom) and current density (bottom, in dashed contour); (b) Mach number (top) and velocity modulus (bottom) distributions with velocity vector overlay, and (c) the near-electrode area is enlarged to show the separation zone. Please note the different scales for the longitudinal and radial axes.

In Figure 9a in the density field, it can be seen that a shock wave was formed in front of the thermal cone. A more detailed view of the flow in the region of the electrodes can be seen in Figure 9b,c, which shows the Mach number and velocity distributions. Regarding the near-electrode region, it is worth noting the presence of a separation flow region near the upstream electrode—the thermal region was an obstacle for the supersonic flow (as, due to the high temperature, a significant subsonic zone was formed). On the other hand, in the hot region between the electrodes, there was an increase in velocity caused by the heating of the gas. Moreover, the downstream electrode had one more area where the speed modulus grew. It was associated with a decrease in the cross-section of the subsonic flow region by the electrode.

As various effects and significant gradients of parameters took place near the electrodes, it made sense to consider and compare them with the obtained experimental data of the values and radial distribution characteristics of the main part of the discharge (more than 5 mm from the electrodes). That is why the main values, such as the maximum

temperature in the discharge and the radial distribution characteristic of the discharge, were considered in a section spaced 15 mm from the electrodes, i.e., in the middle of the discharge gap.

For all obtained distributions of quantities, a good qualitative agreement was achieved between the simulation results in FlowVision and Plasmaero. However, for the main quantities, a quantitative agreement was obtained for the current density, except for the temperature field, for which the difference in the hottest zone exceeded 2000 K, as shown in Figure 10.

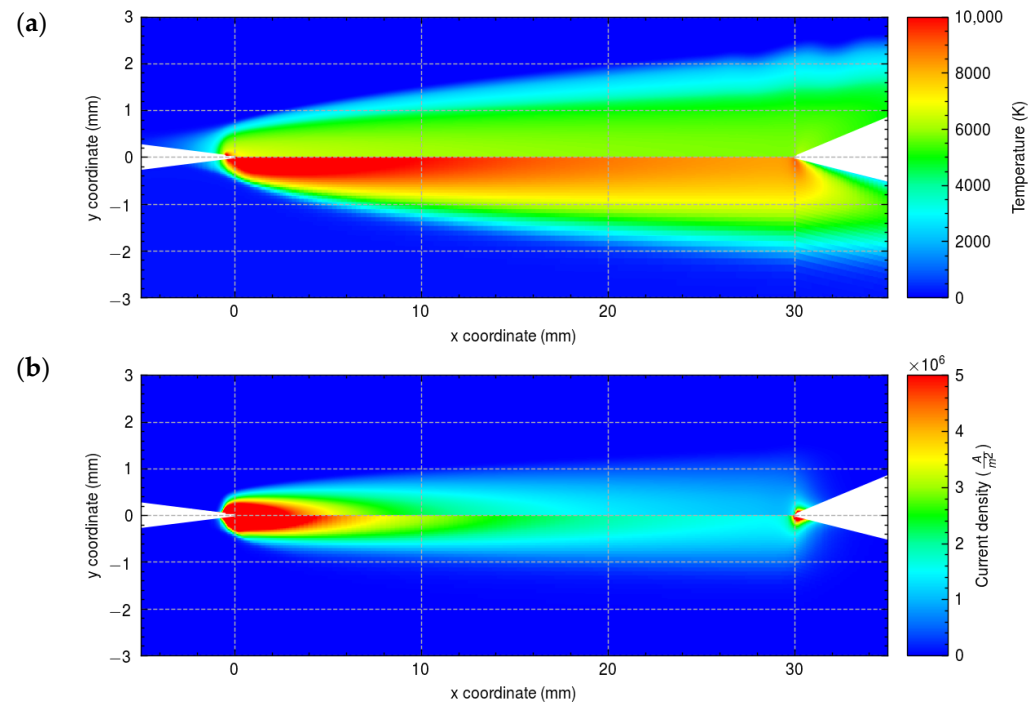


**Figure 10.** The 2D distribution of temperature (a) and current density (b) at  $I = 5$  A obtained in FlowVision (top) and Plasmaero (bottom).

### 5.3. Featured Plasmaero Results

Qualitatively, the gas–dynamic flow fields in Plasmaero were similar to FlowVision and the experiments. The current heated the gas between the electrodes due to the Joule heat, the flow was decelerated and mainly flowed around this heated area, and a separation zone appeared at the left electrode. The gas velocity between the electrodes near the axis was higher than the velocity of the incoming flow, but it was still subsonic on the axis between the electrodes.

The difference in temperature data between Plasmaero and FlowVision can be explained by the use of a highly simplified equilibrium model of air [35] in FlowVision, where the heat capacity and thermal conductivity were given as functions of temperature. The heat capacity increased strongly with temperatures above 5000 K, thus simulating the cost of dissociating molecular nitrogen  $\text{N}_2$ . In FlowVision, this process was immediate; in Plasmaero, it was important how long the molecular nitrogen stayed in the hot zone to obtain the dissociation degree. An additional simulation in Plasmaero was performed using the 0D approach with a fixed temperature  $T = 8000$  K and a density of  $0.01$   $\text{kg/m}^3$  for a mixture of  $0.78\text{N}_2 + 0.22\text{O}_2$ . It was shown that decreasing the  $\text{N}_2$  mole fraction from 0.78 to 0.2 took  $20$   $\mu\text{s}$  (see Figure A1); however, in our 2D simulations of axisymmetric discharge, the time spent by  $\text{N}_2$  in an area with a high temperature was  $25$ – $50$   $\mu\text{s}$ , depending on the simulation case; the density of the axis was  $0.004$ – $0.008$   $\text{kg/m}^3$ . The longitudinal distributions of  $\text{N}_2$  and the N mole fractions at  $r = 0.7$  mm are presented in Figure 11, supplemented with a velocity profile to demonstrate the dynamics of the  $\text{N}_2$  dissociation in the discharge area.

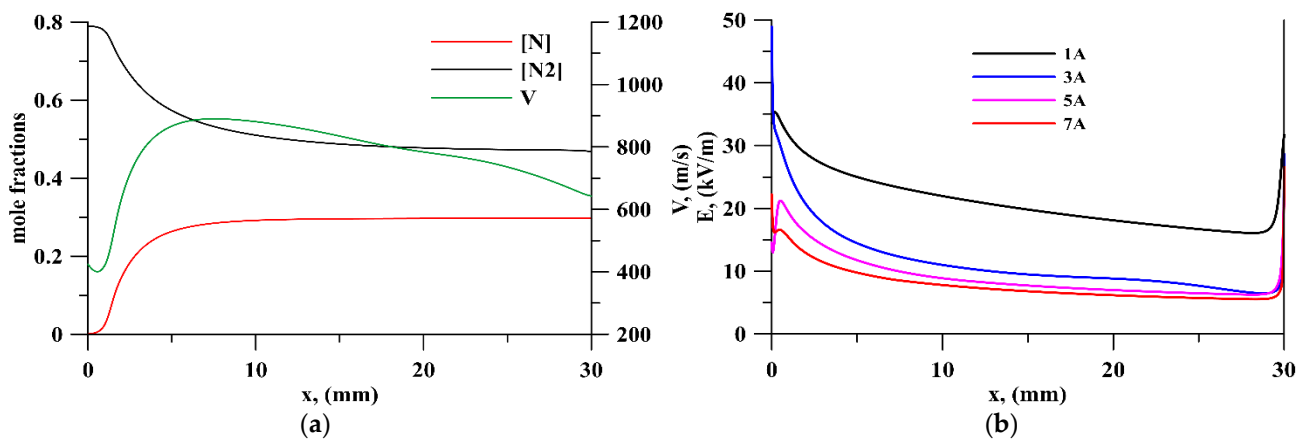


**Figure 11.** Longitudinal distributions of  $N_2$  and  $N$  mole fractions supplemented with a velocity profile for  $r = 0.7$  mm and a discharge current of 5 A (a); longitudinal distribution of the electric field at  $r = 0$  mm (b).

In the gap between the electrodes, the electrical field decreased monotonically (except for the regions near the electrodes) and decreased with the increasing current, as shown in Figure 11b. It can be seen that, in terms of electrical characteristics, mode 1A was very different from the other three cases. A higher field resulted in a higher reduced field. In this case, because of the function of the electron temperature from the reduced field changes, the growth rate starting from the reduced field, 60–70 Td, which ultimately gave the maximum electron temperature of 19,000 K, was compared with 15,000 K at the other currents (see Figure 8).

The key feature that distinguishes Plasmaero from FlowVision for combustion problems is the ability to use detailed plasma–chemical kinetics in conjunction with gas dynamics. The main components in the discharge zone calculated using Plasmaero are shown in Figure 12. It can be seen from the presented distributions that molecular oxygen almost completely dissociated, while the amount of molecular nitrogen decreased insignificantly. The main ion was the  $NO^+$  ion, which also indicated that the chemical equilibrium was not reached for this temperature. In the above-discussed 0D calculation, the mole fraction of  $O^+$  and  $N^+$  ions exceeded the mole fraction of  $NO^+$  after 40  $\mu$ s and 60  $\mu$ s, respectively (see Figure A1). It is also important to note that in the 0D calculation, the mole fraction of atomic oxygen increased rapidly, but gradually decreased over time as the amount of atomic nitrogen increased. Thus, the non-equilibrium nature of the plasma was an advantage, retaining a higher mole fraction of atomic oxygen.

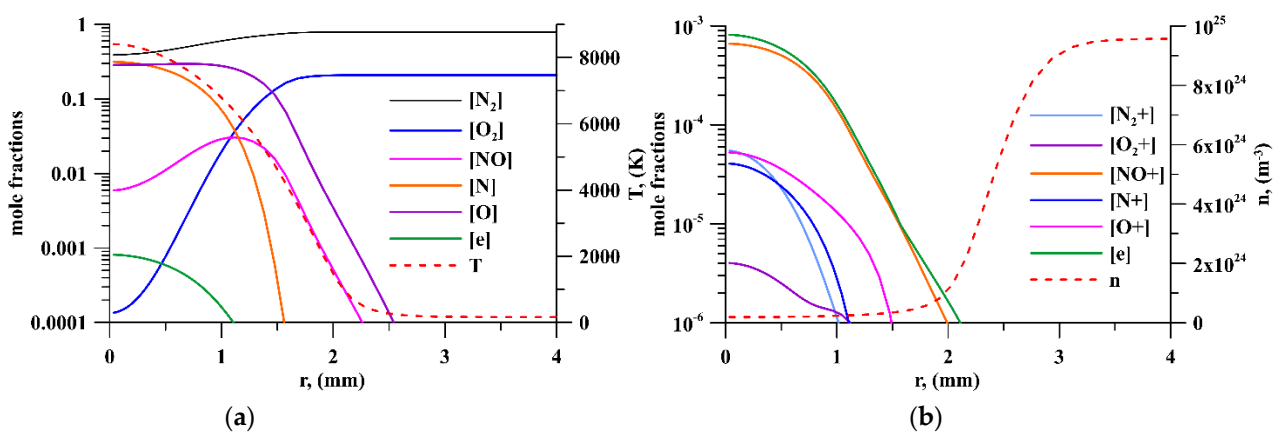


**Figure 12.** Distributions of neutral (a) and charged (b) components, as well as the temperature and concentration for the cross-section (35 mm) and current (5 A).

Despite the fact that only air kinetics, without fuel, were used in the axisymmetric calculation, it was still possible to estimate the potential of the considered discharge for combustion applications. Nonequilibrium plasma could initiate the combustion of a hydrocarbon mixture in two ways: through heating and the creation of active radicals, which significantly accelerate combustion chain reactions. In the chosen scheme of air kinetics, there is a key radical used for accelerating combustion—atomic oxygen. Preliminary estimates made in a zero-dimensional calculation for a mixture of air with ethylene showed that at mixture temperatures of 500–1000 K and an oxygen molar fraction of 0.001–0.1, there was a significant acceleration of reactions, as well as the possibility of ignition during the ‘presence time’ of the mixture in a combustion chamber. It is also worth noting that in the presence of hydrocarbon fuel, atomic oxygen quickly forms intermediate compounds with it, and does not recombine into a molecule when the temperature in the flow decreases after passing through the discharge zone. Figure 13 shows the 2D distributions of the mole fraction of O atoms and temperature, and radial distributions for a cross-section of 45 mm. It can be seen that O atoms were present in a noticeable amount, including where heating was insufficient for ignition, but there was no increase in the molar fraction of oxygen with an increase in the current over 3 A due to full dissociation of O<sub>2</sub>.

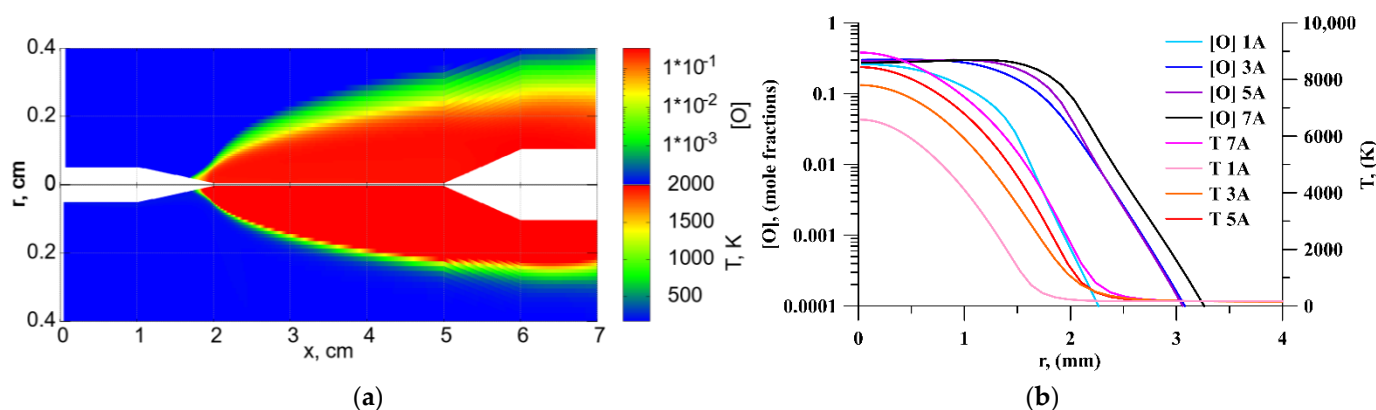


**Figure 13.** The 2D distribution of atomic oxygen (top) and temperature (bottom) (a); radial distributions for the 44 mm section (b) for current 5 A.

## 6. Conclusions

The local and integral characteristics of a direct current’s electric discharge in a supersonic flow (Mach number,  $M = 2$ ) located longitudinally to the flow between the coaxial electrodes were experimentally considered, using simulations via FlowVision and Plasmaero. It was shown that the average discharge temperature increased fast to  $\sim 5500$  K at 1 A, and then rose slower to  $\sim 7500$  K at 7 A due to N<sub>2</sub> dissociation, which increased the effective heat capacity and thermal conductivity of the mixture. However, the discharge plasma was chemically nonequilibrium, which could provide some benefits for combustion enhancement. Thus, a significant mole fraction of atomic oxygen is formed in the discharge and persists after the mixture leaves the discharge region. We can conclude that the increase in the discharge current of more than 3 A at the discussed flow parameters ( $M = 2$ ,  $T_g = 170$  K,  $P_{st} = 22$  kPa), in terms of plasma chemistry, should have no significant additional effects on combustion because the molecular oxygen is already dissociated.

The results obtained by the three methods are in good agreement with each other. All variances are explained by non-equilibrium and contractions of the discharge. For contracted filamentary discharges at the described parameters of 1–7 A, the temperature measured by emission spectroscopy should be perceived as average. The comparison between the simulation and experiment was very important due to the validations of both CFD codes for plasma aerodynamics tasks. Both software packages can be further tested to simulate plasma-assisted combustion. FlowVision is of interest because it allows simulating the electrical discharge in a supersonic flow in a three-dimensional approach accompanied

by simplified combustion chemistry. Plasmaero is of interest due to the detailed plasma chemistry available for discharge and plasma-assisted combustion simulation in a high-speed flow. The use of Plasmaero is limited by 2D or an axisymmetric case, but it could be used for tests of reduced chemical models for further use for plasma-assisted combustion in FlowVision. In this paper, we recognize the results obtained in Plasmaero as more accurate and more complete due to its multi-reaction chemistry; however, the results in FlowVision were obtained much faster due to the execution of calculations in parallel mode. This approach can also be applied to solve three-dimensional problems.

**Author Contributions:** Conceptualization, project oversight, experimental investigation, data analysis, and original draft preparation, A.F.; numerical simulations using Plasmaero, V.B.; numerical simulations using FlowVision, D.T.; CFD data analysis, text editing, A.D.; experimental investigation and data processing, R.T.; Plasmaero development and consultations, A.B. All authors have read and agreed to the published version of the manuscript.

**Funding:** This work was supported by the Russian Science Foundation, grant № 21-79-10408.

**Data Availability Statement:** Data are available upon reasonable request.

**Acknowledgments:** The authors thank S.B. Leonov and I.A. Moralev for the useful consultations, as well as K.V. Savelkin for his help in the preparation and performing of the experiments.

**Conflicts of Interest:** The authors declare no conflict of interest.

## Appendix A

Basic equations of the Plasmaero CFD model.

$$\frac{\partial \rho}{\partial t} + \nabla(\rho \mathbf{U}) = 0$$

$$\frac{\partial \rho \mathbf{U}}{\partial t} + \nabla(\rho \mathbf{U} \cdot \mathbf{U}) + \nabla \tau = -\partial P / \partial r$$

$$\frac{\partial \rho e^0}{\partial t} + \nabla(\rho e^0 + P) \mathbf{U} + \nabla q + \nabla(\mathbf{U} \tau) = j \mathbf{E}$$

$$\frac{\partial \rho_i}{\partial t} + \nabla(\rho_i \cdot \mathbf{U}) + \nabla \Gamma_i = \omega_i$$

$$\nabla j = 0$$

Fluxes

$$\Gamma_i = -\rho D_i \frac{\partial Y_i}{\partial r}$$

$$q - \lambda \frac{\partial T}{\partial r} + \sum_{i \neq e} h_i \Gamma_i$$

$$\tau_{ij} = \frac{2}{3} \eta \delta_{ij} \nabla \mathbf{U} - \eta \left( \frac{\partial u_i}{\partial x_j} + \frac{\partial u_j}{\partial x_i} \right)$$

$$j = \sigma \mathbf{E}; \mathbf{E} = -\frac{\partial \phi}{\partial r}$$

State equations

$$e^0 = e + \frac{U^2}{2}; P = \sum \rho_i R_i T$$

$$e = \sum_{i=1}^{N_1} e_i^0 + \sum_{v=1}^{N_v} e_v + \sum_{i=1}^{N_1^+} e_i^1 + \sum_{i=1}^{N_2^+} e_i^2 + e_e; \rho = \sum \rho_i; c_i = \frac{\rho_i}{W_i}$$



## Chemical kinetics

$$\omega_i = W_i \sum_{r=1}^{N_r} [v''_{i,r} - v'_{i,r}] \cdot \left( k_{fr} \prod_{l=1}^N c_l^{v'_{l,r}} - k_{br} \prod_{l=1}^N c_l^{v''_{l,r}} \right)$$

$$k_{fr} = a \cdot T^b \cdot \exp(-E_a/T); \quad k_{br} = a \cdot T_e^b \cdot \exp(-E_a/T_e)$$

## Electrophysics

$$\sigma = en_e \mu_e; \quad \mu_e = e \frac{\tau_e}{m_e}; \quad \tau_e = \nu_e^{-1}; \quad \nu_e = \sum v_{ej}; \quad v_{ej} = n_j u_e Q_{ej}$$

## Appendix B

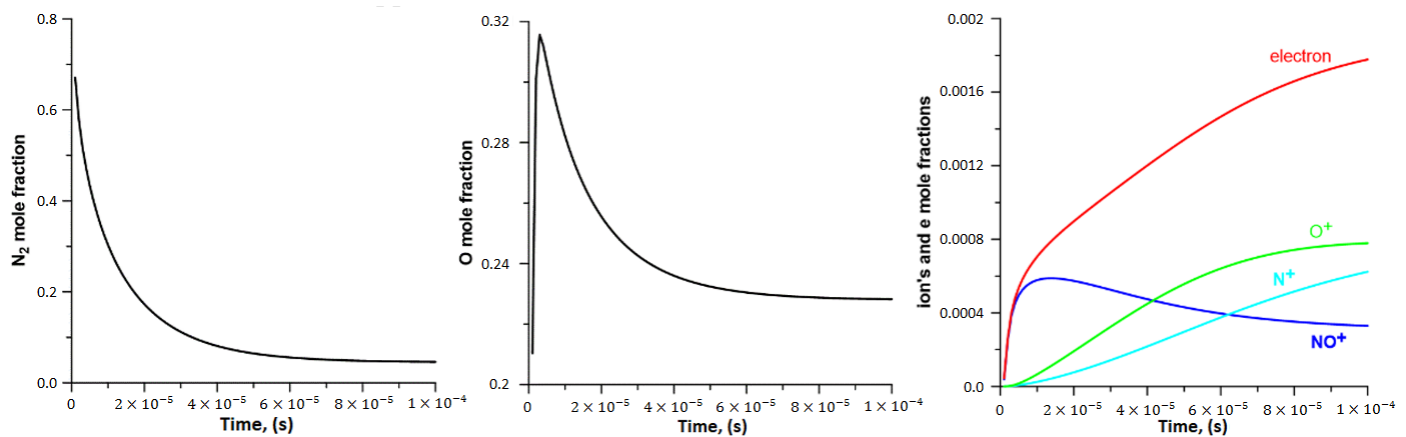


**Figure A1.** Time dependencies of N<sub>2</sub>, O and charged particle mole fractions in the 0D simulation using Plasmaero.

## References

- Caruana, D. Plasmas for Aerodynamic Control. *Plasma Phys. Control. Fusion* **2010**, *52*, 124045. [\[CrossRef\]](#)
- Knight, D.D. *Energy Deposition for High-Speed Flow Control*; Cambridge University Press: Cambridge, UK; New York, NY, USA, 2019; Volume 47, ISBN 1108605516.
- Starikovskiy, A.Y.; Aleksandrov, N.L. Gasdynamic Flow Control by Ultrafast Local Heating in a Strongly Nonequilibrium Pulsed Plasma. *Plasma Phys. Rep.* **2021**, *47*, 148–209. [\[CrossRef\]](#)
- Firsov, A.A.; Shurupov, M.A.; Yarantsev, D.A.; Leonov, S.B.; Shneider, M.N. Mixing Actuation by Unstable Filamentary Discharge. In Proceedings of the 51st AIAA Aerospace Sciences Meeting including the New Horizons Forum and Aerospace Exposition, Grapevine, TX, USA, 7–10 January 2013; p. 1188. [\[CrossRef\]](#)
- Dolgov, E.V.; Kolosov, N.S.; Firsov, A.A. The Study of the Discharge Influence on Mixing of Gaseous Fuel Jet with the Supersonic Air Flow. *Comput. Res. Modeling* **2019**, *11*, 849–860. [\[CrossRef\]](#)
- Firsov, A.A.; Efimov, A.V.; Kolosov, N.S.; Moralev, I.A.; Leonov, S.B. Intensification of Mixing of Fuel with Supersonic Air Flow When Injection and Electric Discharge Are Combined. *J. Phys. Conf. Ser.* **2021**, *2100*, 012007. [\[CrossRef\]](#)
- Feng, R.; Sun, M.; Wang, H.; Huang, Y.; Tian, Y.; Wang, C.; Liu, X.; Zhu, J.; Wang, Z. Experimental Investigation of Flameholding in a Cavity-Based Scramjet Combustor by a Multi-Channel Gliding Arc. *Aerosp. Sci. Technol.* **2022**, *121*, 107381. [\[CrossRef\]](#)
- Leonov, S.B.; Elliott, S.; Carter, C.; Houpt, A.; Lax, P.; Ombrello, T. Modes of Plasma-Stabilized Combustion in Cavity-Based M = 2 Configuration. *Exp. Therm. Fluid Sci.* **2021**, *124*, 110355. [\[CrossRef\]](#)
- Leonov, S. Electrically Driven Supersonic Combustion. *Energies* **2018**, *11*, 1733. [\[CrossRef\]](#)
- Cai, Z.; Wang, T.; Sun, M. Review of Cavity Ignition in Supersonic Flows. *Acta Astronaut.* **2019**, *165*, 268–286. [\[CrossRef\]](#)
- Liu, Q.; Baccarella, D.; Lee, T. Review of Combustion Stabilization for Hypersonic Airbreathing Propulsion. *Prog. Aerosp. Sci.* **2020**, *119*, 100636. [\[CrossRef\]](#)
- Kourtzanidis, K.; Dufour, G.; Rogier, F. Self-Consistent Modeling of a Surface AC Dielectric Barrier Discharge Actuator: In-Depth Analysis of Positive and Negative Phases. *J. Phys. D Appl. Phys.* **2020**, *54*, 045203. [\[CrossRef\]](#)
- Moralev, I.; Ustinov, M.; Kotvitskii, A.; Popov, I.; Selivonin, I.; Kazanskii, P. Stochastic Disturbances, Induced by Plasma Actuator in a Flat Plate Boundary Layer. *Phys. Fluids* **2022**, *34*, 054117. [\[CrossRef\]](#)
- Znamenskaya, I.; Chernikov, V.; Azarova, O. Dynamics of Shock Structure and Frontal Drag Force in a Supersonic Flow Past a Blunt Cone under the Action of Plasma Formation. *Fluids* **2021**, *6*, 399. [\[CrossRef\]](#)

15. Znamenskaya, I.A.; Dolbnya, D.I.; Ivanov, I.E.; Kuli-zade, T.A.; Sysoev, N.N. Pulse Volume Discharge behind Shock Wave in Channel Flow with Obstacle. *Acta Astronaut.* **2022**, *195*, 493–501. [[CrossRef](#)]
16. Mursenkova, I.V.; Ivanov, I.E.; Liao, Y.; Kryukov, I.A. Experimental and Numerical Investigation of a Surface Sliding Discharge in a Supersonic Flow with an Oblique Shock Wave. *Energies* **2022**, *15*, 2189. [[CrossRef](#)]
17. Zhang, C.B.; Yang, H.; Liang, H.; Guo, S.G. Plasma-Based Experimental Investigation of Double Compression Ramp Shock Wave/Boundary Layer Interaction Control. *J. Phys. D Appl. Phys.* **2022**, *55*, 325202. [[CrossRef](#)]
18. Leonov, S.B.; Firsov, A.A.; Yarantsev, D.A.; Falempin, F.; Miller, A. Flow Control in Model Supersonic Inlet by Electrical Discharge. In Proceedings of the 16th AIAA/DLR/DGLR International Space Planes and Hypersonic Systems and Technologies Conference, Bremen, Germany, 19–22 October 2009; p. 7367. [[CrossRef](#)]
19. Watanabe, Y.; Elliott, S.; Firsov, A.; Houpt, A.; Leonov, S. Rapid Control of Force/Momentum on a Model Ramp by Quasi-DC Plasma. *J. Phys. D Appl. Phys.* **2019**, *52*, 444003. [[CrossRef](#)]
20. Firsov, A.; Savelkin, K.V.; Yarantsev, D.A.; Leonov, S.B. Plasma-Enhanced Mixing and Flameholding in Supersonic Flow. *Philos. Trans. R. Soc. A Math. Phys. Eng. Sci.* **2015**, *373*, 20140337. [[CrossRef](#)]
21. Firsov, A.A.; Kolosov, N.S. Combustion in a Supersonic Flow Using a Pylon Equipped with a Plasma Actuator. *J. Phys. Conf. Ser.* **2021**, *2100*, 012017. [[CrossRef](#)]
22. Alferov, V.I.; Bushmin, A.S. Electrical Discharge in a Supersonic Air Flow. *J. Exp. Theor. Phys.* **1963**, *17*, 1775–1779.
23. Shibkova, L.V.; Shibkov, V.M.; Logunov, A.A.; Dolbnya, D.S.; Kornev, K.N. Parameters of Pulsed Discharge Plasma in High-Speed Gas Flows. *High Temp.* **2020**, *58*, 754–760. [[CrossRef](#)]
24. Leonov, B.S.; Hedlund, B.; Houpt, A. Morphology of a Q-DC Discharge within a Fuel Injection Jet in a Supersonic Cross-Flow. In Proceedings of the AIAA Aerospace Sciences Meeting, Kissimmee, FL, USA, 8–12 January 2018; p. 1060. [[CrossRef](#)]
25. Firsov, A.A.; Yarantsev, D.A.; Leonov, S.B. Control of Q-DC Electrical Discharge Position in Supersonic Flow by External Magnetic Field. In Proceedings of the 46th AIAA Plasmadynamics and Lasers Conference, Dallas, TX, USA, 22–26 June 2015; p. 2659. [[CrossRef](#)]
26. Firsov, A.A.; Yarantsev, D.A.; Leonov, S.B.; Ivanov, V.V. Numerical Simulation of Ethylene Combustion in Supersonic Air Flow. *Comput. Res. Modeling* **2017**, *9*, 75–86. [[CrossRef](#)]
27. Efimov, A.V.; Firsov, A.A.; Kolosov, N.S.; Leonov, S.B. Characterization of Electric Discharge Collocated with Gas Jet in Supersonic Airflow. *Plasma Sources Sci. Technol.* **2020**, *29*, 07LT01. [[CrossRef](#)]
28. Moralev, I.; Kazanskii, P.; Bitururin, V.; Bocharov, A.; Firsov, A.; Dolgov, E.; Leonov, S. Gas Dynamics of the Pulsed Electric Arc in the Transversal Magnetic Field. *J. Phys. D Appl. Phys.* **2020**, *53*, 425203. [[CrossRef](#)]
29. Rakhimov, R.G.; Moralev, I.A.; Firsov, A.A.; Bitururin, V.A.; Bocharov, A.N. On the Gasdynamics of the Electric Discharge in External Magnetic Field. *J. Phys. Conf. Ser.* **2019**, *1147*, 012128. [[CrossRef](#)]
30. Bitururin, V.A.; Bocharov, A.N.; Kuznetsova, T.N. Numerical Simulation of an Axisymmetric Discharge in a Supersonic Air Co-Flow. *J. Phys. Conf. Ser.* **2020**, *1698*, 012027. [[CrossRef](#)]
31. Gray, M.D.; Sirohi, J.; Raja, L.L. Modeling and Physical Analysis of Rail Plasma Actuator Arc. In Proceedings of the 2018 AIAA Aerospace Sciences Meeting, Kissimmee, FL, USA, 8–12 January 2018; p. 0935. [[CrossRef](#)]
32. Bourlet, A.; Labaune, J.; Tholin, F.; Pechereau, F.; Vincent-Randonnier, A.; Laux, C.O. Numerical Model of Restrikes in DC Gliding Arc Discharges. In Proceedings of the AIAA SCITECH 2022 Forum, San Diego, CA, USA, 3–7 January 2022; p. 831. [[CrossRef](#)]
33. Aksenov, A.A. FlowVision: Industrial Computational Fluid Dynamics. *Comput. Res. Modeling* **2017**, *9*, 5–20. [[CrossRef](#)]
34. FlowVision User Manual. Available online: [https://flowvisioncfd.com/webhelp/fven\\_31204/](https://flowvisioncfd.com/webhelp/fven_31204/) (accessed on 14 September 2022).
35. D'Angola, A.; Colonna, G.; Gorse, C.; Capitelli, M. Thermodynamic and Transport Properties in Equilibrium Air Plasmas in a Wide Pressure and Temperature Range. *Eur. Phys. J. D* **2007**, *46*, 129–150. [[CrossRef](#)]
36. Tarasov, D.A.; Firsov, A.A. CFD Simulation of DC-Discharge in Airflow. *J. Phys. Conf. Ser.* **2021**, *2100*, 012015. [[CrossRef](#)]
37. Bitururin, V.A.; Bocharov, A.N. MHD Heat Flux Mitigation in Hypersonic Flow around a Blunt Body with Ablating Surface. *J. Phys. D Appl. Phys.* **2018**, *51*, 264001. [[CrossRef](#)]
38. Bitururin, V.A.; Bocharov, A.N. Magnetohydrodynamic Interaction in Hypersonic Air Flow Past a Blunt Body. *Fluid Dyn.* **2006**, *41*, 843–856. [[CrossRef](#)]
39. Bitururin, V.A.; Bocharov, A.N.; Popov, N.A. Numerical Simulation of an Electric Discharge in Supersonic Flow. *Fluid Dyn.* **2008**, *43*, 642–653. [[CrossRef](#)]
40. Leakey, S.; Glenis, V.; Hewett, C.J.M. A Novel Godunov-Type Scheme for Free-Surface Flows with Artificial Compressibility. *Comput. Methods Appl. Mech. Eng.* **2022**, *393*, 114763. [[CrossRef](#)]
41. Gustafsson, I. On Modified Incomplete Factorization Methods. In *Numerical Integration of Differential Equations and Large Linear Systems. Lecture Notes in Mathematics*; Hinze, J., Ed.; Springer: Berlin/Heidelberg, Germany, 1982; Volume 968, pp. 334–351. [[CrossRef](#)]
42. Park, C. Review of Chemical-Kinetic Problems of Future NASA Missions. I: Earth Entries. *J. Thermophys. Heat Transf.* **2012**, *7*, 385–398. [[CrossRef](#)]
43. Popov, N.A. Fast Gas Heating in a Nitrogen–Oxygen Discharge Plasma: I. Kinetic Mechanism. *J. Phys. D Appl. Phys.* **2011**, *44*, 285201. [[CrossRef](#)]

- 
44. Pusateri, E.N.; Morris, H.E.; Nelson, E.M.; Ji, W. Determination of Equilibrium Electron Temperature and Times Using an Electron Swarm Model with BOLSIG+ Calculated Collision Frequencies and Rate Coefficients. *J. Geophys. Res. Atmos.* **2015**, *120*, 7300–7315. [[CrossRef](#)]
  45. Shibkov, V.M.; Shibkova, L.V.; Logunov, A.A. Parameters of the Plasma of a Dc Pulsating Discharge in a Supersonic Air Flow. *Plasma Phys. Rep.* **2017**, *43*, 373–380. [[CrossRef](#)]